Check for updates

Recombination in Passivating Contacts: Investigation Into the Impact of the Contact Work Function on the Obtained Passivation

Anh Huy Tuan Le, Ruy S. Bonilla, Lachlan E. Black, Johannes P. Seif, Thomas G. Allen, Robert Dumbrell, Christian Samundsett, and Ziv Hameiri*

Improving the passivation of contacts in silicon solar cells is crucial for reaching high-efficiency devices. Herein, the impact of the contact work function on the obtained passivation is examined and quantified using a novel method—quasi-steady-state photoluminescence—which provides access to the surface saturation current density after metallization ($J_{0s,m}$). The obtained $J_{0s,m}$ indicates an improvement of the surface passivation when contacts with high work function are applied onto Si wafers passivated with aluminum oxide, regardless of the wafer doping type. This improvement is mainly due to the amplification of the imbalance between the electron and hole concentrations near the Si interface. The passivation quality is reduced when using contacts with low work function in which the recombination rate increases via the charge-assisted carrier population control. Herein, the vital importance of selecting suitable metals to minimize contact recombination in high-efficiency solar cells is pointed.

1. Introduction

Recombination losses of photo-generated carriers at the contacts of crystalline silicon (c-Si) solar cells have been one of the main factors limiting their power conversion efficiency.[1–3] Such losses are usually caused by direct contact between the metal and the Si wafer which induces interfacial defects, the so-called metal-induced gap states (MIGS).[4–9] A well-known approach to reduce the impact of this recombination is to minimize the contact area, as is done in the passivated emitter and rear locally diffused (PERL) and the passivated emitter and rear totally diffused (PERT) cells.[10,11] Nevertheless, even when the metal/Si contact area fraction is minimized to less than 1%, the recombination at this interface can still dominate the overall recombination due to the extremely high surface recombination velocity ($>10^5$ cm s^{-1}) at the contacts.[3,12] This is especially critical in current high-efficiency devices, since the overall passivation of the free surface is remarkably good; hence, the contacts are becoming a roadblock to the improvement of cell efficiency. To further reduce this loss, an alternative approach has been developed using the so-called passivating contacts.[13–18] These contacts are typically composed of a thin passivation layer and a carrier-selective layer, which are inserted between the Si wafer and the metal.[1–3] The former layer is used to passivate the wafer surface by reducing the concentration of interfacial defects and/or creating an asymmetric population of majority and minority carriers.[12,19] The carrier-selective layer is used to collect either electrons or holes from the bulk.[12,19] Critically, in all proposed passivating contact cell architectures, the contacting metal is separated from the c-Si absorber, minimizing MIGS.[6]

The imbalance between the surface concentrations of electrons (n_s) and holes (p_s) can be obtained by using 1) a doping profile at the interface, 2) charge-assisted population control, and 3) work-function population control.[19] The first approach is usually obtained by diffusion of dopant atoms; however, this leads to both a narrowing of the bandgap and an increase in Auger recombination within the highly doped regions.[3] The second approach can be achieved using a highly charged film that attracts carriers of opposite polarity.[12] The third method is based on the deposition of a material with a different work function

A. H. T. Le, J. P. Seif, Z. Hameiri
School of Photovoltaic and Renewable Energy Engineering
University of New South Wales
Sydney, NSW 2052, Australia
E-mail: huytuananh.le@unsw.edu.au

R. S. Bonilla
Department of Materials
University of Oxford
Oxford OX1 3PH, UK

L. E. Black, C. Samundsett
School of Engineering
The Australian National University
Canberra ACT 2600, Australia

T. G. Allen
KAUST Solar Center (KSC)
Physical Sciences and Engineering Division (PSE)
King Abdullah University of Science and Technology
Thuwal 23955-6900, Saudi Arabia

R. Dumbrell
Zhejiang Jinko Solar Co., Ltd.
Haining, Zhejiang 314416, China

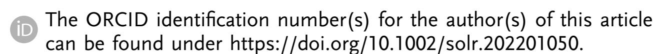
The ORCID identification number(s) for the author(s) of this article can be found under https://doi.org/10.1002/solr.202201050.

© 2023 The Authors. Solar RRL published by Wiley-VCH GmbH. This is an open access article under the terms of the Creative Commons Attribution-NonCommercial-NoDerivs License, which permits use and distribution in any medium, provided the original work is properly cited, the use is non-commercial and no modifications or adaptations are made.

DOI: 10.1002/solr.202201050

compared to the c-Si substrate, resulting in a higher concentration of one type of carrier near the interface.[20] Therefore, it is expected that the work function of the metal applied as a contact will impact the carrier concentrations near the interface and hence the surface recombination rate.

Indeed, the impact of the contact work function on the carrier populations near the Si surface was observed in Si heterojunction solar cells.[21,22] A dependency of the band bending near the Si surface on the work function of transparent conductive oxide (TCO) layers, which behave as a metal, was reported in Refs. [21,22]. Van de Loo et al.[23] reported variations in the injection-dependent minority carrier lifetime (τ_{eff}) of c-Si wafers passivated by stacks of silicon dioxide, zinc oxide, and aluminum oxide (AlO_x) films as a function of the ZnO doping level. More relevant, using photoluminescence images, Matsui et al.[20] showed that the work function of metal contacts deposited on a 5-nm titanium oxide (TiO_x) layer (used as a passivating contact) significantly impacts the surface passivation quality regardless of the wafer polarity. Significant degradation of the surface passivation was noticed when an Al layer was used for *p*-type devices.[20] These results indicate that the contact work function influences the surface recombination statistics despite the interlayer between the contact and the Si. However, no direct evidence, such as a variation of the surface saturation current density (J_{0s}) before and after metallization, has been presented, mainly since common lifetime measurement techniques have severe limitations when applied to metallized samples.

The J_{0s} is often used as a figure of merit to assess the interface passivation quality.[24] For nonmetallized structures, J_{0s} can be easily extracted from τ_{eff} obtained from photo-conductance (PC) measurements using the Kane–Swanson method.[24] However, the extraction of the surface saturation current density of metallized structures ($J_{0s,m}$) using the same technique is challenging due to the significantly larger conductivity of metals compared to that of c-Si. Several alternative approaches to extract $J_{0s,m}$ have been reported;[25–27] however, each approach has its own limitations, as discussed in Refs. [28,29]. Recently, a robust and contactless method based on the quasi-steady-state photoluminescence (QSSPL) technique has been suggested to obtain τ_{eff} of any metallized structure.[28,29] This method, therefore, provides access to $J_{0s,m}$.

In this study, we investigate the impact of the contact work function on the surface passivation using QSSPL measurements. For this purpose, the chemical passivation layer needs to 1) be sufficiently thin (ideally ≤5 nm) to ensure that the impact of the contact work function is not significantly attenuated and hence an apparent trend can be observed and 2) supply a good surface passivation and thus the obtained $J_{0s,m}$ is sufficiently sensitive to the variation of the contact work function. The impact of the contact work function is then quantified based on the ratio between J_{0s} (before metallization) and $J_{0s,m}$ (after metallization). Moreover, a numerical model is established to validate the experimental results.

2. Experimental Section

2.1. Sample Preparation

Commercial *p*-type (resistivity: 1.8–2.0 Ω cm, thickness: 180 ± 10 μm) and *n*-type (resistivity: 5.8–6.4 Ω cm, thickness: 180 ± 10 μm) Czochralski-grown Si wafers were used in this study. The wafers were RCA (Radio Corporation of America) cleaned[30] and then dipped in hydrofluoric acid to remove the native oxide prior to atomic layer deposition (ALD; Beneq TFS 200) of AlO_x using trimethylaluminum and deionized water at 200 °C. Two test structures were used, as shown in **Figure 1**. For all the structures, 20-nm AlO_x films were deposited on one side ("front") of the wafers. Films with a thickness of either 20 nm (Structure A) or 5 nm (Structure B) were then deposited on the opposite side ("rear"). All the samples were annealed at 400 °C prior to the deposition of contacts. Contact layers with different work functions were then thermally evaporated on the rear side of Structures A and B to form Structures A_m and B_m. **Table 1** provides the information regarding the materials used for the contact layers. In this study, AlO_x layers were used as the chemical passivation layer. Compared to SiO_2 films, these layers provided better surface passivation at thicknesses below 5 nm. For instance, the effective surface recombination velocity (S_{eff}) obtained on *n*-type Si wafers passivated by our 5-nm AlO_x layers was in the range of 4–6 cm s^{-1}, compared to S_{eff} of 60–70 cm s^{-1} reported for those passivated by 5-nm SiO_x films.[31]

Note that the work functions of *n*- and *p*-type Si wafers were determined based on the model suggested by Altermatt et al.,[32] assuming an ionization of 100% and 99.5%, respectively.

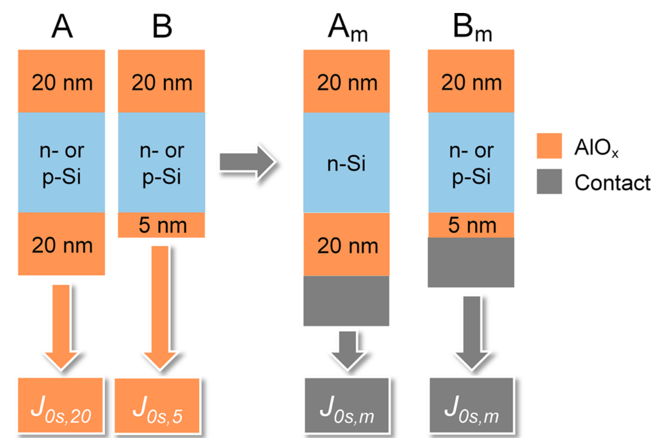

Figure 1. Schematics of the test structures to extract J_{0s} and $J_{0s,m}$.

Table 1. Work function of the different contact materials, the *p*- and *n*-type c-Si substrates.

Materials	Work function [eV]	Remark
Lithium fluoride/aluminum (LiF/Al)	2.86	[16]
Magnesium (Mg)	3.66	[62]
Al	4.20	[62]
n-Si	4.37	Calculated
Silver (Ag)	4.74	[62]
p-Si	5.01	Calculated
Palladium (Pd)	5.22	[62]
Molybdenum oxide (MoO_x)/Ag	5.70	[16]

© 2023 The Authors. Solar RRL published by Wiley-VCH GmbH

2367198x, 2023, 11, Downloaded from https://onlinelibrary.wiley.com/doi/10.1002/solr.202201050 by Test, Wiley Online Library on [20/09/2023]. See the Terms and Conditions (https://onlinelibrary.wiley.com/terms-and-conditions) on Wiley Online Library for rules of use; OA articles are governed by the applicable Creative Commons License

2367198x, 2023, 11, Downloaded from https://onlinelibrary.wiley.com/doi/10.1002/solr.202201050 by Test, Wiley Online Library on [20/09/2023]. See the Terms and Conditions (https://onlinelibrary.wiley.com/terms-and-conditions) on Wiley Online Library for rules of use; OA articles are governed by the applicable Creative Commons License

2.2. Characterization

For the nonmetallized samples (Structures A and B), τ_{eff} was measured using both a standard lifetime tester (WCT-120, Sinton Instruments) and the QSSPL technique, whereas the metallized samples (Structure B_m) were measured only by the latter.[28,29] In the latter technique, the emitted PL was generated by illuminating the samples using an 808-nm diode laser before being collected by an optical system. The injection-dependent τ_{eff} was then determined from the time-dependent measurements of the PL intensity. Further details of the measurement setup for this technique can be found in Ref. [28].

The J_{0s} of the Si surface passivated by 20-nm AlO_x films ($J_{0s,20}$) was extracted from Structure A using the injection-dependent τ_{eff} curve fitting model of Quokka 2[33] and the approach of Dumbrell et al.[28] In this model, an equal front and rear J_{0s} and a constant bulk Shockley–Read–Hall lifetime (τ_{SRH}, valid at high injection levels, $>5 \times 10^{15}$ cm^{-3} for the n-type Si wafers and $>8 \times 10^{15}$ cm^{-3} for the p-type Si wafers) were used as fitting parameters. For the asymmetrically passivated samples (Structures B and B_m), the previously fitted $J_{0s,20}$ and the constant bulk SRH lifetime were fixed, while the rear J_{0s} was fitted to obtain J_{0s} of the Si surface passivated by 5-nm AlO_x films ($J_{0s,5}$) and $J_{0s,m}$. The calculation of the intrinsic lifetime was based on the model of Richter et al.,[34] while the effective intrinsic carrier concentration ($n_{i,eff}$, 9.65×10^9 cm^{-3}) was determined using the models of Schenk[35] and Altermatt et al.[36]

2.3. Modeling

An interface recombination model[37] was developed based on the extended Shockley–Read–Hall formalism,[38] combined with the iterative algorithms of Girisch et al.[39] and Aberle et al.[40] The model incorporated the effect of charge fluctuations[37] and considered the effect of the contact work function by assuming that the metal effectively forms a gate contact in a metal–oxide-semiconductor (MOS) structure with a short-circuited (zero bias) electrical connection between the gate and the c-Si substrate. This was equivalent to assuming that the charge transfer, driven by the work-function difference, can occur between the metal and the substrate (as dielectrics are not perfect electrical insulators). Transient recharging effects during illumination were not considered in this model since they would require knowledge of the exact nature of all defects, which was not available in most cases. The Si space-charge density was calculated following the methods presented in Refs. [38,41]. The input parameters for this model were described as follows.

1) The fixed charges (Q_f) within the AlO_x films and the density of interfacial defects (D_{it}) were obtained from contactless capacitance–voltage measurements.[42]

2) In the ALD process, a silicon oxide (SiO_x) interlayer was inevitably formed between the Si wafer and the AlO_x film.[43–45] As a result, a SiO_x/Si interface was considered in the developed model. The defect distributions at this interface were chosen based on experimental values reported in Refs. [46,47] such that the overall defect densities were representative of a physical interface. Regarding Q_f, it was demonstrated by Hiller et al.[43] that it was located at the two-dimensional AlO_x/SiO_x interface.

3) Top-hat distributions for both donors and acceptors. By using these distributions, the entire bandgap can be covered, thus, reproducing the experimentally measured distribution of states at the interface. Gaussian distributions were also tested. However, the obtained results do not match well with the experimental results as when top-hat distributions are used (see Appendix A).

4) Tail states: It is well known that band tails are always present at the semiconductor–dielectric interface as they arise from terminating the periodicity of the crystal at the surface.[48,49] They substantially affect the balance of charge at the interface[46,47] and their presence slightly impacts the absolute value of J_{0s} and its trend as a function of the contact work function.

The input parameters are summarized in **Table 2**. Note that the width of the tail distribution is defined as the energy gap between the band edge and the energy at which the defect density decreased to below 10^8 cm^{-2} eV^{-1} (see Appendix B for details).

The electron and hole capture cross sections (σ_n and σ_p, respectively) of both the donor and acceptor top-hat defects were fitted to reproduce the experimental results. The fitting quality was assessed based on the obtained 1) J_{0s} values before metallization ($J_{0s,5}$, 40–45 fA cm^{-2} for the n-type and 30–35 fA cm^{-2} for the p-type test structures) and 2) trend of the $J_{0s,m}/J_{0s,5}$ ratio as a function of contact work function. The obtained parameters are summarized in **Table 3**.

Table 4 compares σ_n and σ_n/σ_p obtained in this study and previously reported values. Note that in Refs. [50,51], only the σ_n/σ_p ratios near mid-gap were given as the energy dependence of capture cross sections were considered. It was noticeable that the reported ranges for σ_n and σ_n/σ_p spread across two orders of magnitude (between 1.4×10^{-16} and 1.5×10^{-14} cm^2 for σ_n and 2 and 100 for σ_n/σ_p). Our values

Table 2. Input parameters used in the model including experimentally measured Q_f and D_{it} for the AlO_x films of 5 nm. These measured D_{it} values are used as D_{it} of the donor top-hat and acceptor top-hat defects.

		p-type Si	n-type Si
	Wafer thickness [μm]—measured	180 ± 10	
	Wafer doping [cm^{-3}]—measured	$(7.1–7.9) \times 10^{15}$	$(7.0–7.7) \times 10^{14}$
	Dielectric constant of AlO_x	8	
	Q_f [cm^{-2}]—measured	$-(1.4–3.9) \times 10^{12}$	$-(1.1–3.5) \times 10^{12}$
	D_{it} [cm^{-2} eV^{-1}]—measured	$(5.3–7.9) \times 10^{11}$	$(5.0–7.5) \times 10^{11}$
Defects	Donor top-hat—Energy level [eV]	−0.20	
	Donor top-hat—Width [eV]	0.40	
	Acceptor top-hat—Energy level [eV]	0.20	
	Acceptor top-hat—Width [eV]	0.40	
Tail states	Donor tail—Energy level [eV]	−0.56	
	Donor tail—Tail width [eV]	0.30	
	Donor tail—D_{it} [cm^{-2}·eV^{-1}]	1.8×10^{14}	
	Acceptor tail—Energy level [eV]	0.56	
	Acceptor tail—Tail width [eV]	0.30	
	Acceptor tail—D_{it} [cm^{-2} eV^{-1}]	1.8×10^{14}	

© 2023 The Authors. Solar RRL published by Wiley-VCH GmbH

Table 3. Best-fit interfacial defect parameters for test structures using both *n*- and *p*-type wafers.

	Donor top-hat	Acceptor top-hat
σ_n [cm^{-2}]	$(4.0 \pm 2.1) \times 10^{-15}$	$(1.0 \pm 0.5) \times 10^{-15}$
σ_p [cm^{-2}]	$(4.0 \pm 2.1) \times 10^{-16}$	$(2.6 \pm 1.4) \times 10^{-14}$

Table 4. σ_n and σ_n/σ_p at the SiO_x/Si interface obtained from the model in this study and reported in the literature.

Reference	Treatment	Substrate	ρ [Ω cm]	σ_n [cm^2]	σ_n/σ_p
This study	–	*n*-type Cz	1.8-2	4.0×10^{-15}	10
[63]	–	*n*-type FZ[a)]	1	1.4×10^{-16}	2
[37]	–	*n*-type	1	8.7×10^{-16}	7.9
[52]	–	*n*-type FZ	2-3	7.5×10^{-15}	2.3
[63]	FGA[b)]	*n*-type FZ	1	1.4×10^{-16}	2
[37]	FGA	*n*-type	1	7.7×10^{-16}	13.4
[52]	FGA	*p*-type FZ	2-3	1.5×10^{-14}	5.2
[50]	FGA	*p*-type FZ	1	–	100
[51]	Post-metallization anneal	*p*-type	1	–	50-70

a)FZ: Float zone. b)FGA: Forming gas annealing.

were within these ranges and are similar to those reported by Refs. [37,52].

The S_{eff} was extracted at the excess carrier concentration (Δn) of 10^{15} cm^{-3} and is calculated using the following equation[53]

$$\frac{1}{\tau_{eff}} = \frac{1}{\tau_{int}} + \frac{1}{\tau_{SRH}} + \frac{2S_{eff}}{W} \tag{1}$$

where τ_{int} is the intrinsic lifetime (determined using the model of Ref. [34]), and W is the wafer thickness. The obtained S_{eff} represents its upper limit as τ_{SRH} was assumed to have only a negligible contribution to τ_{eff}. The simulated and measured τ_{eff} as a function of Δn of the *n*- and *p*-type test structures before metallization (Structure B) are compared in Figure 1C (see Appendix C). A good agreement between those $\tau_{eff}(\Delta n)$ curves was observed, confirming the validity of the developed model.

3. Results and Discussion

3.1. Validation of Quasi-Steady-State Photoluminescence τ_{eff} Measurements

To confirm the validity of the QSSPL method, τ_{eff} measurements of the nonmetallized samples (Structure B) taken by PL- and PC-based method were compared. A representative example is shown in **Figure 2**. The uncertainty associated with the QSSPL measurement was determined considering the uncertainty of input parameters following the method of Ref. [54], while the uncertainty associated with the PC-based measurement was calculated using the approach of McIntosh et al.[55] The difference in J_{0s} extracted from these two methods is below 9%. The same

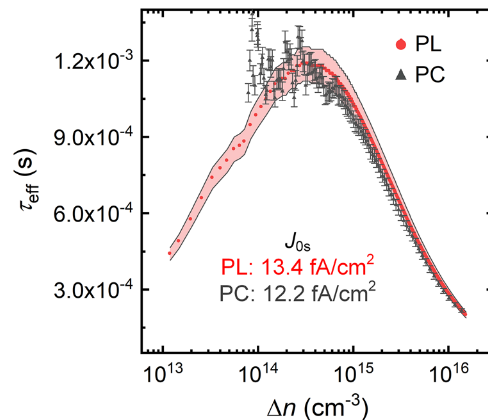

Figure 2. Injection-dependent τ_{eff} data of Structure B measured by the QSSPC and QSSPL methods. The red zone shows the standard deviation of QSSPL measurements in which 68% of data points lie.

method (of Ref. [54]) was used in the rest of the study to determine the uncertainty of the extracted J_{0s} and hence of the ratio of $J_{0s,m}$ to $J_{0s,5}$.

3.2. Impact of the Contact Work Function

The experimental $J_{0s,m}/J_{0s,5}$ ratios of the *n*-type test structures as a function of the contact work function are shown in **Figure 3**a. A ratio smaller than one indicates an improvement of the surface passivation after metallization and vice versa. As can be seen, when applying high-work-function contacts (work function higher than that of c-Si), the surface passivation is improved. For low-work-function contacts (work function lower than that of c-Si), the improvement is less pronounced. It is noticeable that the quality of the surface passivation is reduced if a Mg contact with a work function of 3.66 eV is used, as will be discussed later.

The figure also includes the simulated results. There is a good qualitative agreement between the experimental and simulated trends of J_{0s} ratio as a function of contact work function. It demonstrates that the work function of contacts indeed influences the carrier populations near the interface and hence the recombination statistics, despite an interlayer (an AlO_x film in this study) with a thickness of up to 5 nm between the contact and the Si. It is noticeable that the variation of the $J_{0s,m}/J_{0s,5}$ ratio as a function of contact work function shows a higher magnitude in the simulated data. This difference can be explained by the following phenomena. First, it is well known that the Schottky barrier height at the Si/metal interface—which derives from the difference in the electron (hole) concentration between the Si wafer and metal—strongly depends on the interfacial defects causing a pinning of the Fermi level.[56,57] This effect influences the Schottky barrier height, but it does not influence the trend of the variation of the barrier height with contact work function. In this study, despite the presence of the AlO_x passivation layer, D_{it} is relatively high [(5.0–7.9) $\times 10^{11}$ cm^{-2} eV^{-1}] and sufficient to limit the movement of the Fermi level.[58] A second possible mechanism is the influence of a surface dipole at the metal–dielectric interface.[59] The contributions from such the

© 2023 The Authors. Solar RRL published by Wiley-VCH GmbH

2367198x, 2023, 11, Downloaded from https://onlinelibrary.wiley.com/doi/10.1002/solr.202201050 by Test, Wiley Online Library on [20/09/2023]. See the Terms and Conditions (https://onlinelibrary.wiley.com/terms-and-conditions) on Wiley Online Library for rules of use; OA articles are governed by the applicable Creative Commons License

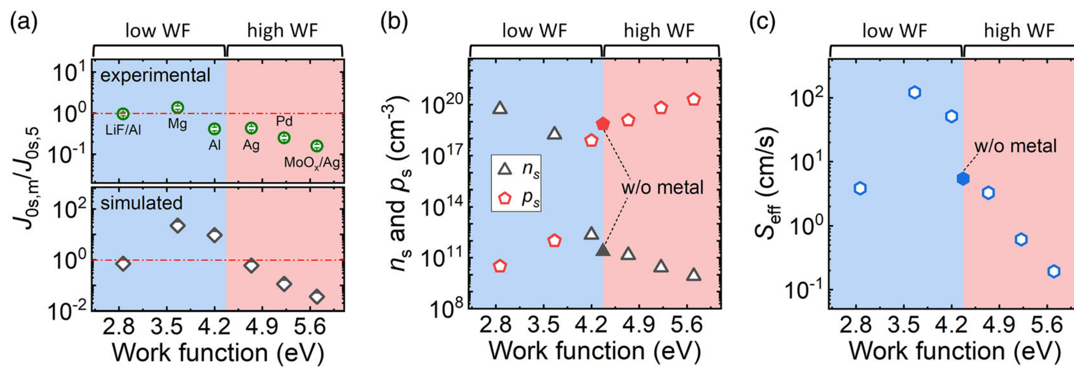

Figure 3. a) Experimental and simulated $J_{0s,m}/J_{0s,5}$ ratios as a function of work function for the *n*-type test structures, b) calculated n_s and p_s, and c) simulated S_{eff} before (solid symbols) and after (open symbols) metallization. Error bars in (a) are determined by the uncertainty of QSSPL measurements as shown in Figure 2.

dipole to the work functions of the metal and semiconductor are not considered in our model since they depend on the unknown interface electronic structure.[60] Another possibility is that the actual contact work functions are lower than the values listed in Table 1. However, the results in Appendix D indicate that this cannot explain the observed difference. As our model does not consider either Fermi-level pinning or surface dipoles, we, therefore, attribute the difference between the modeled and measured results to these effects.

To gain a deeper understanding regarding the work-function-dependent behavior of the $J_{0s,m}/J_{0s,5}$ ratios, the calculated n_s and p_s before and after metallization are presented in Figure 3b. As the AlO_x films have a finite resistance, electrons unavoidably transfer between the Si wafer and the metal contact to reach a lower energy level, provided sufficient time has passed. As mentioned above, in this model, it is assumed that there is a charge transfer between the Si wafer and the contact despite the AlO_x layer of 5 nm between them. The surface potential difference is then given by the work function difference. As expected, before metallization (solid symbols), p_s is dominant due to the presence of negative charges in the AlO_x films, inducing a depletion region near the Si surface. After metallization (open symbols), p_s is still dominant when contacts exhibiting a high work function are used. In this case, the asymmetric population of electrons and holes is amplified, resulting in a significant reduction in the surface recombination rate. When applying contacts with lower work functions, the hole accumulation region is neutralized and the dominance of p_s is less pronounced. With a further decrease in the work function, n_s increases and becomes dominant. An electron accumulation region is formed when the asymmetric population of electrons and holes is further amplified. The change of the dominant carrier population from holes to electrons at the interface indicates a change in the polarity of the Si surface potential from negative to positive. The impact of the contact work function on the carrier populations is, therefore, similar to the effect of the fixed charges in the passivation layers.

From Figure 3b, the work-function-dependent behavior of the calculated n_s and p_s is illustrated. The S_{eff} is determined using the model and depicted in Figure 3c to provide more information about the recombination statistics near the interface. For comparison, the experimental values of S_{eff} for *n*-type test structures before metallization are in the range of 4–6 cm s^{-1}. It can be clearly seen that the trend of the calculated S_{eff} as a function of contact work function shows a good qualitative agreement with those of the experimental and simulated $J_{0,sm}/J_{0s,5}$ ratios. The determined S_{eff} is highest when using a contact with a work function of 3.66 eV although the imbalance of the n_s and p_s at this point is not the lowest value [see Figure 3b]. This is due to the asymmetry of the obtained σ_n and σ_p of the interfacial defects.

The experimental $J_{0,sm}/J_{0s,5}$ ratios of the *p*-type test structures as a function of contact work function are shown in **Figure 4**a. Similar to the *n*-type case, the surface passivation is improved when applying high-work-function contacts. As discussed earlier, this is attributed to the amplification of the imbalance between n_s and p_s near the Si surface. When applying lower-work-function contacts, this improvement is less pronounced. The surface passivation is degraded with a 4.2 eV work function contact (Al) before improving again with a further decrease in the contact work function. Matsui et al.[20] also reported a significant degradation of the surface passivation when using Al contacts for devices with *p*-type Si wafers, which is in good agreement with our results.

The figure also presents the simulated results. Similar to the case with n-Si wafers, the trend of the simulated and experimental results in Figure 4a shows a good qualitative agreement. The larger change is predicted by the model and again attributed to a combination of Fermi-level pinning and surface dipole effects. Note that the good qualitative agreement between the trends of the simulated and experimental results is achieved using the same interfacial parameters in both the *n*- and the *p*-type cases, further strengthening our conclusions.

Using a similar modeling approach, the calculated n_s and p_s before and after metallization are presented in Figure 4b. Before metallization (solid symbols), p_s is dominant due to the presence of negative charges in AlO_x films, resulting in a hole accumulation region near the surface. It is still dominant when applying contacts with high work functions and the imbalance between n_s and p_s is amplified, resulting in a significant reduction of the recombination rate. This supports the observed improvement of surface passivation with increasing

© 2023 The Authors. Solar RRL published by Wiley-VCH GmbH

2367198x, 2023, 11, Downloaded from https://onlinelibrary.wiley.com/doi/10.1002/solr.202201050 by Test, Wiley Online Library on [20/09/2023]. See the Terms and Conditions (https://onlinelibrary.wiley.com/terms-and-conditions) on Wiley Online Library for rules of use; OA articles are governed by the applicable Creative Commons License

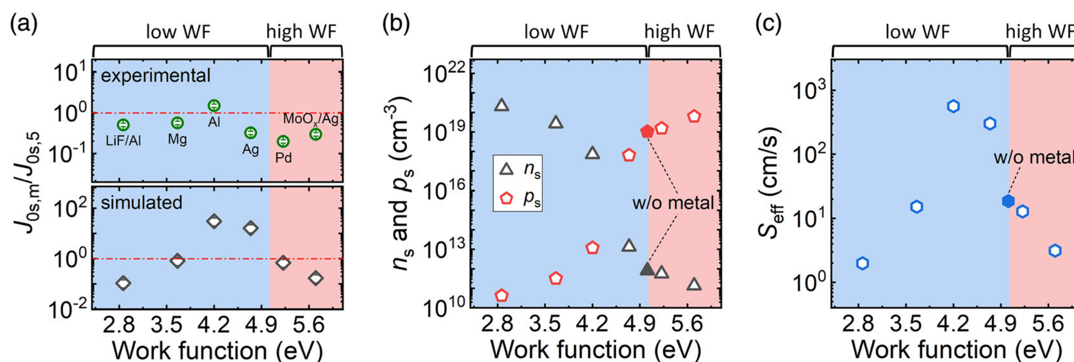

Figure 4. a) Experimental and simulated $J_{0s,m}/J_{0s,5}$ ratios as a function of work function for the *p*-type test structures, b) calculated n_s and p_s, and c) simulated S_{eff} before (solid symbols) and after (open symbols) metallization. Error bars in (a) are determined by the uncertainty of QSSPL measurements as shown in Figure 2.

the contact work function as shown in Figure 4a. As expected, n_s increases when applying contacts with lower work functions. It becomes dominant with a further decrease of the work function, indicating a change in the polarity of the Si surface potential from positive to negative.

The S_{eff} values calculated using n_s and p_s in Figure 4b together with the interface model are depicted in Figure 4c as a function of contact work function. For comparison, the experimental values of S_{eff} for *p*-type test structures before metallization are in the range of 16–20 cm s^{-1}. It is also found that the trend of the determined S_{eff} shows a good qualitative agreement with those of the experimental and simulated $J_{0,sm}/J_{0s,5}$ ratios [see Figure 4a]. Due to the asymmetry of σ_n and σ_p for the interfacial defects in the model, we also find the highest S_{eff} at the contact work function of 4.2 eV although the imbalance of the n_s and p_s at this point is not the lowest [see Figure 4b].

To assess the influence of the thickness of the AlO_x films, the experimental $J_{0s,m}$ extracted from Structures A_m (20 nm rear AlO_x) and B_m (5 nm rear AlO_x) is shown in **Figure 5** as a function of contact work function. The $J_{0s,m}$ of Structure A_m is significantly lower than that of Structure B_m. This is due to the improvement of the surface passivation when the thickness of the AlO_x films increases. As expected, $J_{0s,m}$ of Structure A_m (20 nm) is less sensitive to the contact work function.

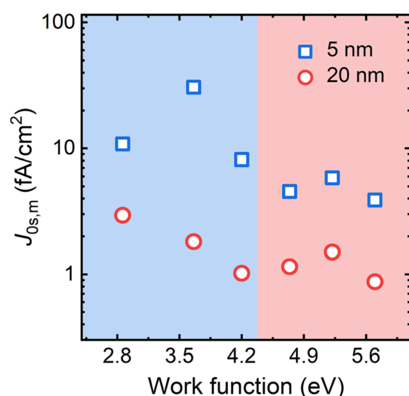

Figure 5. $J_{0s,m}$ extracted from Structures A_m (20 nm rear AlO_x) and B_m (5 nm rear AlO_x) for the *n*-type test structures as a function of work function.

This can be explained by the fact that the electric field in the dielectric (and therefore, the band bending in the Si) required to compensate for the potential difference between the metal and the Si is reduced when increasing the thickness of the dielectric layer.

4. Conclusion

In this study, the QSSPL technique was used to investigate the impact of the contact work function on the surface passivation by extracting J_{0s} at the metal–Si interfaces. It was demonstrated that the surface passivation of Si wafers passivated by AlO_x films is improved by applying contacts with high work function regardless of the wafer polarity. These seem to be the first direct measurements of J_{0s} after metallization (using practical metallization processes). The surface passivation is worsened at certain contact work functions. To benefit from the asymmetric carrier population induced by the contact, it is recommended to apply a contact with a work function that is lower (higher) than the Si work function if positive (negative) fixed charges are present in the passivation layer to amplify the asymmetric carrier population. This study provides useful insights into the influence of contact work function on the obtained passivation and, hence, offers a potential pathway for further improving the performance of solar cells via selecting suitable metals to minimize contact recombination.

Appendix A.

Top-Hat vs Gaussian Distributions

To select an appropriate defect distribution for the model used in this study, two common distributions, top-hat and Gaussian, for both donor-like and acceptor-like defects were compared. The input parameters of the top-hat distributions are listed in Table 2. For the Gaussian distribution, the defect energy level and the peak width for both donor-like and acceptor-like defects are set to the values reported in Ref. [61]. The rest of the input parameters are the same as those listed in Table 2.

© 2023 The Authors. Solar RRL published by Wiley-VCH GmbH

2367198x, 2023, 11, Downloaded from https://onlinelibrary.wiley.com/doi/10.1002/solr.202201050 by Test, Wiley Online Library on [20/09/2023]. See the Terms and Conditions (https://onlinelibrary.wiley.com/terms-and-conditions) on Wiley Online Library for rules of use; OA articles are governed by the applicable Creative Commons License

As discussed earlier, a fit is defined when both the experimental J_{0s} before metallization and the trend of $J_{0s,m}/J_{0s,5}$ ratios as a function of contact work function are simultaneously reproduced. **Figure A1** presents the experimental and fitted $J_{0s,m}/J_{0s,5}$ ratios using Gaussian distributions as a function of contact work function for the *n*-type test structures. The two criteria above cannot be simultaneously satisfied. When an agreement with $J_{0s,5}$ is obtained [see Figure A1a], the simulated trend and the absolute value of $J_{0s,m}/J_{0s,5}$ ratios do not agree well with the experimental data. Meanwhile, when the experimental and fitted $J_{0s,m}/J_{0s,5}$ ratios agree, the simulated $J_{0s,5}$ ($\approx$6 fA cm^{-2}) is significantly smaller than the experimental value (40–45 fA cm^{-2}) [see Figure A1b]. Therefore, the top-hat and band tail defect distributions were used in this study as they appear to better represent the electrical characteristics of the interface.

Simulated $J_{0s,m}/J_{0s,5}$ ratios using Gaussian distributions with and without tail states as well as a top-hat distribution are shown in Figure A1c for comparison. The results indicate that the presence of tail states in the Gaussian distribution does not account for the deviation between the Gaussian and top-hat distributions.

Appendix B.

Defect Distributions

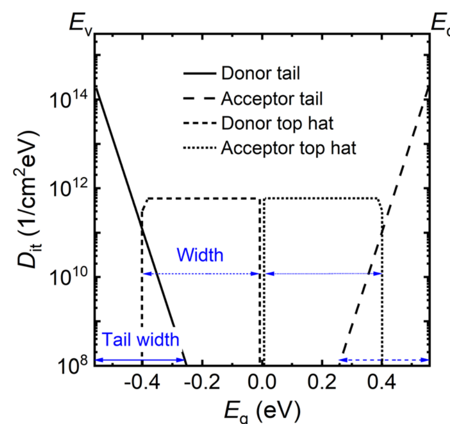

Figure B1. The distribution of defects including donor tail, acceptor tail, donor top-hat, and acceptor top-hat.

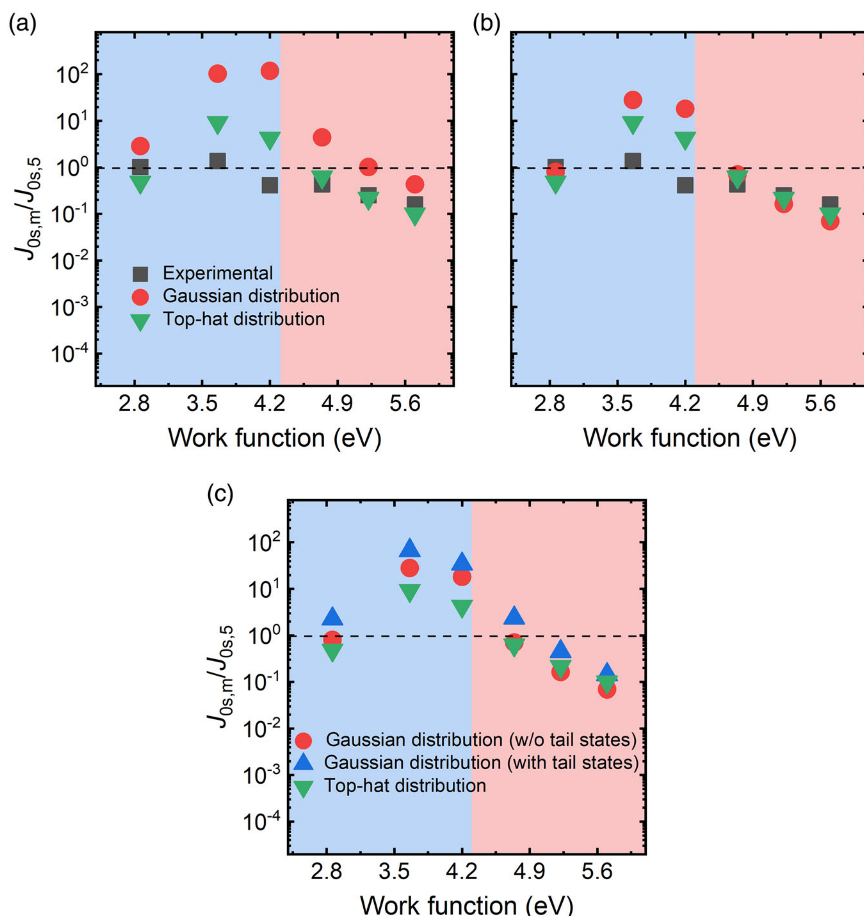

Figure A1. Experimental and simulated $J_{0s,m}/J_{0s,5}$ ratios using Gaussian and top-hat distributions as a function of contact work function for the *n*-type test structures: a) Best fit to match $J_{0s,5}$ (40–45 fA cm^{-2}) and b) best fit to match the trend of the $J_{0s,m}/J_{0s,5}$ ratios as a function of contact work function. c) Simulated $J_{0s,m}/J_{0s,5}$ ratios using Gaussian (with and without tail states) and top-hat distributions.

© 2023 The Authors. Solar RRL published by Wiley-VCH GmbH

2367198x, 2023, 11, Downloaded from https://onlinelibrary.wiley.com/doi/10.1002/solr.202201050 by Test, Wiley Online Library on [20/09/2023]. See the Terms and Conditions (https://onlinelibrary.wiley.com/terms-and-conditions) on Wiley Online Library for rules of use; OA articles are governed by the applicable Creative Commons License

Appendix C.

Measured vs Simulated τ_{eff}

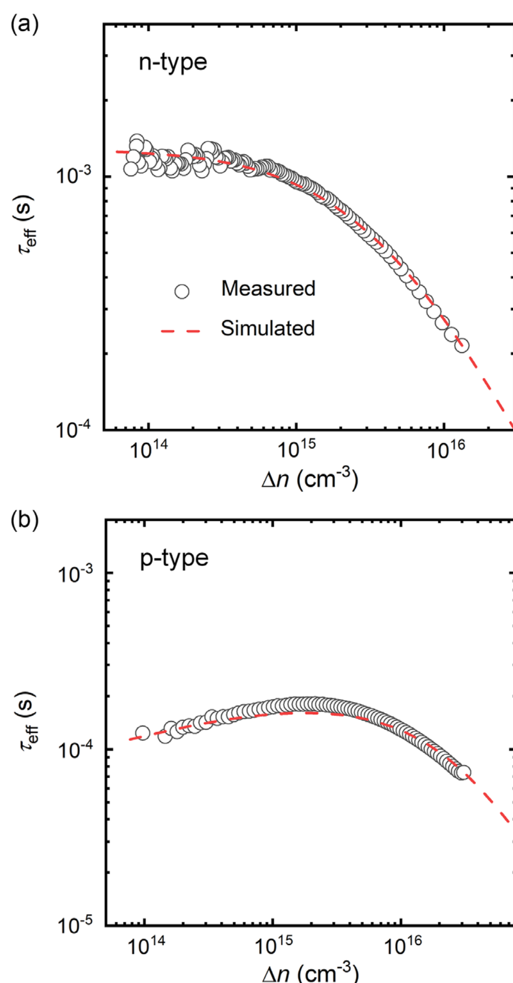

Figure C1. Measured and simulated τ_{eff} as a function of Δn for the a) *n*-type and b) *p*-type test structures before metallization (Structure B).

Appendix D.

Simulations for Lower Work Functions

In Section 3.2, a lesser variation of the $J_{0s,m}/J_{0s,5}$ ratio as a function of contact work function was observed in the experimental results, compared to the simulated data [see Figure 3a and 4a]. Three possible explanations for this observation were proposed: 1) Fermi-level pinning, 2) surface dipoles, and 3) lower actual contact work functions than those used in the simulations (Table 1). To examine the third possibility, simulations were performed where the work functions were assumed to be 5% lower than the values stated in Table 1, and the results are shown in **Figure D1**. Despite the lower work function, the variation of the simulated $J_{0s,m}/J_{0s,5}$ ratio still shows a higher magnitude compared to the experimental results. We, therefore, still attribute the difference in magnitude between the simulated and experimental results to the effects of the Fermi-level pinning and/or surface dipoles, as discussed in Section 3.2. Note that the extremely high J_{0s} ratios at lower work functions of 4.2 eV are due to $n_s \times \sigma_n \approx p_s \times \sigma_p$ at these points.

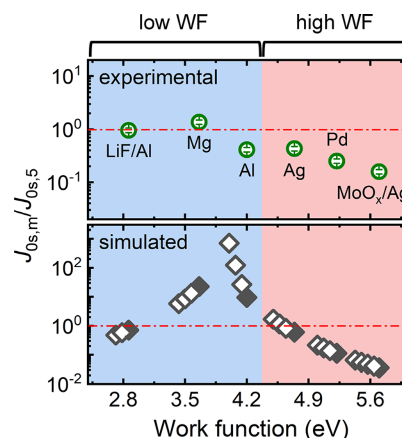

Figure D1. Experimental (top) and simulated (bottom) $J_{0s,m}/J_{0s,5}$ ratios as a function of effective work function for the *n*-type test structures. For the simulated results, solid symbols represent the effective work functions shown in Table 1, whereas open symbols indicate 5% lower work functions.

Acknowledgements

This work was supported by the Australian Government through the Australian Renewable Energy Agency [ARENA; projects 2017/RND001 and 2020/RND016]. R.S.B. was supported by the UK Royal Academy of Engineering under the Research Fellowship Scheme and by the UK Engineering and Physical Sciences Research Council grant number EP/V038605/1. L.E.B. was supported by ARENA [project 2020/RND009]. The views expressed herein are not necessarily the views of the Australian Government, and the Australian Government does not accept responsibility for any information or advice contained herein.

Open access publishing facilitated by University of New South Wales, as part of the Wiley - University of New South Wales agreement via the Council of Australian University Librarians.

Conflict of Interest

The authors declare no conflict of interest.

Data Availability Statement

The data that support the findings of this study are available from the corresponding author upon reasonable request.

Keywords

passivating contacts, quasi-steady-state photoluminescence, saturation current density, silicon solar cells, surface recombination, work function

Received: November 23, 2022
Revised: March 14, 2023
Published online: March 28, 2023

© 2023 The Authors. Solar RRL published by Wiley-VCH GmbH

2367198x, 2023, 11, Downloaded from https://onlinelibrary.wiley.com/doi/10.1002/solr.202201050 by Test, Wiley Online Library on [20/09/2023]. See the Terms and Conditions (https://onlinelibrary.wiley.com/terms-and-conditions) on Wiley Online Library for rules of use; OA articles are governed by the applicable Creative Commons License

[1] T. G. Allen, J. Bullock, X. B. Yang, A. Javey, S. De Wolf, *Nat. Energy* **2019**, *4*, 914.
[2] J. Melskens, B. W. H. van de Loo, B. Macco, L. E. Black, S. Smit, W. M. M. Kessels, *IEEE J. Photovoltaic* **2018**, *8*, 373.
[3] M. Hermle, F. Feldmann, M. Bivour, J. C. Goldschmidt, S. W. Glunz, *Appl. Phys. Rev.* **2020**, *7*, 021305.
[4] A. Agrawal, J. Lin, M. Barth, R. White, B. Zheng, S. Chopra, S. Gupta, K. Wang, J. Gelatos, S. E. Mohney, S. Datta, *Appl. Phys. Lett.* **2014**, *104*, 112101.
[5] D. Connelly, C. Faulkner, D. E. Grupp, J. S. Harris, *IEEE Trans. Nanotechnol.* **2004**, *3*, 98.
[6] M. Sajjad, X. B. Yang, P. Altermatt, N. Singh, U. Schwingenschlogl, S. De Wolf, *Appl. Phys. Lett.* **2019**, *114*, 071601.
[7] C. Tejedor, F. Flores, E. Louis, *J. Phys. C: Solid State Phys.* **1977**, *10*, 2163.
[8] J. Tersoff, *Phys. Rev. B* **1984**, *30*, 4874.
[9] J. Tersoff, *Phys. Rev. B* **1985**, *32*, 6968.
[10] M. A. Green, *Solar Energy Mater. Sol. Cells* **2015**, *143*, 190.
[11] J. H. Zhao, A. H. Wang, M. A. Green, *Prog. Photovoltaics* **1999**, *7*, 471.
[12] J. Schmidt, R. Peibst, R. Brendel, *Solar Energy Mater. Sol. Cells* **2018**, *187*, 39.
[13] J. Bullock, C. Samundsett, A. Cuevas, F. Yan, Y. M. Wan, T. Allen, *IEEE J. Photovoltaic* **2015**, *5*, 1591.
[14] X. B. Yang, P. T. Zheng, Q. Y. Bi, K. Weber, *Solar Energy Mater. Sol. Cells* **2016**, *150*, 32.
[15] J. Bullock, P. T. Zheng, Q. Jeangros, M. Tosun, M. Hettick, C. M. Sutter-Fella, Y. Wan, T. Allen, D. Yan, D. Macdonald, S. De Wolf, A. Hessler-Wyser, A. Cuevas, A. Javey, *Adv. Energy Mater.* **2016**, *6*, 1600241.
[16] J. Bullock, M. Hettick, J. Geissbuhler, A. J. Ong, T. Allen, C. M. Sutter-Fella, T. Chen, H. Ota, E. W. Schaler, S. De Wolf, C. Ballif, A. Cuevas, A. Javey, *Nat. Energy* **2016**, *1*, 15031.
[17] M. Tanaka, M. Taguchi, T. Matsuyama, T. Sawada, S. Tsuda, S. Nakano, H. Hanafusa, Y. Kuwano, *Jpn. J. Appl. Phys.* **1992**, *31*, 3518.
[18] F. Feldmann, M. Simon, M. Bivour, C. Reichel, M. Hermle, S. W. Glunz, *Appl. Phys. Lett.* **2014**, *104*, 181105.
[19] A. Cuevas, Y. M. Wan, D. Yan, C. Samundsett, T. Allen, X. Y. Zhang, J. Cui, J. Bullock, *Solar Energy Mater. Sol. Cells* **2018**, *184*, 38.
[20] T. Matsui, S. McNab, R. S. Bonilla, H. Sai, *ACS Appl. Energy Mater.* **2022**, *5*, 12782.
[21] R. Rößler, C. Leendertz, L. Korte, N. Mingirulli, B. Rech, *J. Appl. Phys.* **2013**, *113*, 144513.
[22] E. Centurioni, D. Iencinella, *IEEE Electron Device Lett.* **2003**, *24*, 177.
[23] B. Van De Loo, B. Macco, J. Melskens, W. Beyer, W. Kessels, *J. Appl. Phys.* **2019**, *125*, 105305.
[24] D. Kane, R. Swanson, in *18th IEEE Photovoltaic Specialists Conf.,* IEEE, Piscataway, NJ **1985**, pp. 578–583.
[25] V. Shanmugam, T. Mueller, A. G. Aberle, J. Wong, *Sol. Energy* **2015**, *118*, 20.
[26] A. Fell, D. Walter, S. Kluska, E. Franklin, K. Weber, *Energy Proc.* **2013**, *38*, 22.
[27] T. Fellmeth, A. Born, A. Kimmerle, F. Clement, D. Biro, R. Preu, *Energy Proc.* **2011**, *8*, 115.
[28] R. Dumbrell, M. K. Juhl, T. Trupke, Z. Hameiri, *IEEE J. Photovolt.* **2018**, *8*, 1413.
[29] R. Dumbrell, M. K. Juhl, M. Li, T. Trupke, Z. Hameiri, in *44th IEEE Photovoltaic Specialist Conf.,* IEEE, Piscataway, NJ **2017**, pp. 3315–3318.
[30] W. Kern, *J. Electrochem. Soc.* **1990**, *137*, 1887.
[31] N. E. Grant, K. R. McIntosh, in *24th European Photovoltaic Solar Energy Conf.*, IEEE, Piscataway, NJ **2009**, pp. 1676–1679.
[32] P. Altermatt, A. Schenk, G. J. Heiser, *Appl. Phys.* **2006**, *100*, 113715.
[33] A. Fell, *IEEE Trans. Electron Dev.* **2012**, *60*, 733.
[34] A. Richter, S. W. Glunz, F. Werner, J. Schmidt, A. Cuevas, *Phys. Rev. B* **2012**, *86*, 165202.
[35] A. Schenk, *J. Appl. Phys.* **1998**, *84*, 3684.
[36] P. P. Altermatt, A. Schenk, F. Geelhaar, G. Heiser, *J. Appl. Phys.* **2003**, *93*, 1598.
[37] R. S. Bonilla, I. Al-Dhahir, M. Yu, P. Hamer, P. P. Altermatt, *Sol. Energy Mater. Sol. Cells* **2020**, *215*, 110649.
[38] A. Grove, D. Fitzgerald, *Solid State Electron.* **1966**, *9*, 783.
[39] R. B. Girisch, R. P. Mertens, R. F. De Keersmaecker, *IEEE Trans. Electron Dev.* **1988**, *35*, 203.
[40] A. G. Aberle, S. Glunz, W. Warta, *J. Appl. Phys.* **1992**, *71*, 4422.
[41] C. E. Young, *J. Appl. Phys.* **1961**, *32*, 329.
[42] M. Wilson, J. Lagowski, L. Jastrzebski, A. Savtchouk, V. Faifer, *AIP Conf. Proc.* **2001**, *550*, 220.
[43] D. Hiller, D. Tröger, M. Grube, D. König, T. Mikolajick, *J. Phys. D* **2021**, *54*, 275304.
[44] B. Hoex, S. Heil, E. Langereis, M. Van de Sanden, W. Kessels, *Appl. Phys. Lett.* **2006**, *89*, 042112.
[45] Y. Etinger-Geller, E. Zoubenko, M. Baskin, L. Kornblum, B. Pokroy, *J. Appl. Phys.* **2019**, *125*, 185302.
[46] M. Yu, S. McNab, I. Al-Dhahir, C. E. Patrick, P. P. Altermatt, R. S. Bonilla, *Sol. Energy Mater. Sol. Cells* **2021**, *231*, 111307.
[47] R. S. Bonilla, P. R. Wilshaw, *J. Appl. Phys.* **2017**, *121*, 135301.
[48] F. Giustino, A. Pasquarello, *Surf. Sci.* **2005**, *586*, 183.
[49] S. Markov, P. Sushko, C. Fiegna, E. Sangiorgi, A. Shluger, A. Asenov, *J. Phys.: Conf. Ser.* **2010**, *242*, 012010.
[50] S. Glunz, D. Biro, S. Rein, W. Warta, *J. Appl. Phys.* **1999**, *86*, 683.
[51] A. Aberle, S. Glunz, A. Stephens, M. Green, *Prog. Photovolt.* **1994**, *2*, 265.
[52] H. Haug, S. Olibet, Ø. Nordseth, E. Stensrud Marstein, *J. Appl. Phys.* **2013**, *114*, 174502.
[53] R. Eberle, A. Fell, T. Niewelt, F. Schindler, M. C. Schubert, *AIP Conf. Proc.* **2019**, *2147*, 140001.
[54] Z. Hameiri, K. R. McIntosh, T. Trupke, in *38th IEEE Photovoltaic Specialists Conf.,* IEEE, Piscataway, NJ **2012**, pp. 000390–000395.
[55] K. R. McIntosh, R. A. Sinton, in *23rd European Photovoltaic Solar Energy Conf.*, IEEE, Piscataway, NJ **2008**, pp. 77–82.
[56] R. Tung, *J. Vac. Sci. Technol. B* **1993**, *11*, 1546.
[57] W. Mönch, *Surf. Sci.* **1970**, *21*, 443.
[58] R. Schlaf, R. Hinogami, M. Fujitani, S. Yae, Y. Nakato, *J. Vac. Sci. Technol. A* **1999**, *17*, 164.
[59] E. Roderick, R. Williams, in *Metal–Semiconductor Contacts*, Clarendon Press, Oxford **1988**.
[60] R. T. Tung, *Mater. Sci. Eng., R* **2001**, *35*, 1.
[61] L. E. Black, K. R. McIntosh, *IEEE J. Photovoltaic* **2013**, *3*, 936.
[62] D. R. Lide, in *CRC Handbook of Chemistry and Physics*, 90th ed., Vol. *2*, CRC Press, Taylor & Francis Group, Boca Raton, FL **2010**.
[63] S. Nie, R. S. Bonilla, Z. Hameiri, *Solar Energy Mater. Sol. Cells* **2021**, *224*, 111021.

© 2023 The Authors. Solar RRL published by Wiley-VCH GmbH

2367198x, 2023, 11, Downloaded from https://onlinelibrary.wiley.com/doi/10.1002/solr.202201050 by Test, Wiley Online Library on [20/09/2023]. See the Terms and Conditions (https://onlinelibrary.wiley.com/terms-and-conditions) on Wiley Online Library for rules of use; OA articles are governed by the applicable Creative Commons License